



Graphene aerogel-based NiAl-LDH/g-C₃N₄ with ultratight sheet-sheet heterojunction for excellent visible-light photocatalytic activity of CO₂ reduction

Min Yang^a, Peng Wang^a, Youji Li^{a,*}, Senpei Tang^{b,*}, Xiao Lin^{b,*}, Haiyan Zhang^b, Zi Zhu^b, Feitai Chen^{a,*}

^a National Experimental Teaching Demonstration Center for Chemistry, Jishou University, Jishou 416000, PR China

^b College of Chemistry and Chemical Engineering, Jishou University, Jishou 416000, PR China

ARTICLE INFO

Keywords:

NiAl-LDH/g-C₃N₄
Sheet-sheet heterojunctions
Graphene aerogel
CO₂ photoreduction
Visible light

ABSTRACT

NiAl-LDH (NALDH) nanosheets were in intimate contact with g-C₃N₄ (CN) nanosheets to form ultratight sheet-sheet heterojunctions, which interweaved into network framework with introduction of the graphene aerogel (GA). Notably, the NALDH/CN/GA-20 showed a remarkable CO production rate of 28.83 $\mu\text{mol}\cdot\text{g}^{-1}\cdot\text{h}^{-1}$ under visible light irradiation, which was 24 and 16 times those of pure NALDH and bare CN, respectively. Furthermore, it was far exceeding the reported conventional CO₂ photocatalytic reduction efficiency. The ultratight sheet-sheet heterojunctions not only shorten the charge transmission distance, but result abundant active sites and coupling large interfaces. The unique structure promoted the transport and separation of photogenerated carriers, and facilitated effective mass transport and light absorption. Multi electron series reduction mechanism based on type-II photocatalytic system was proposed to explain the CO₂ reduction pathway. This work provides insight for designing photocatalysts with ideal performance for CO₂ reduction.

1. Introduction

In recent years, owing to the rapid industrialization of society, humans are facing increasing challenges, such as the climate and energy crises. Greenhouse gas emissions and fossil fuel depletion have resulted in an urgent search for solutions to meet societal energy needs [1–3]. Photocatalytic technology can effectively utilize abundant solar energy to convert CO₂ into valuable fuels, such as CO, CH₄, CH₃OH, HCOOH, and HCHO, which can alleviate both the greenhouse effect and energy crisis [4,5]. In 1979, Inoue et al. [6] discovered that CO₂ could be reduced to hydrocarbon fuels in aqueous solution containing suspended semiconductor particles under illumination. The subsequent study of photocatalytic CO₂ reduction has attracted extensive research attention. However, CO₂ exhibits chemical inactivity and high thermal stability owing to its extremely high bond energy (750 kJ·mol⁻¹). CO₂ photocatalytic reduction is not only a thermodynamic process, but also faces enormous kinetic challenges [7,8]. Therefore, identifying catalysts with high activity, selectivity, and stability is important. Notably, only a few photocatalysts can be effectively applied, with most semiconductors

severely limited owing to wide energy bands, low solar energy efficiency, or rapid recombination of photogenerated charge carriers [9–12]. Catalysts have been modified to improve their photocatalytic activity and product selectivity. The most effective method involves constructing a complex semiconductor heterojunction, which can reduce the recombination of electron-hole pairs, enhance charge separation and transport, and expand the light absorption range [13–17].

Layered double hydroxides (LDH) are two-dimensional (2D) layered inorganic multifunctional compounds [18]. As LDHs exhibit highly uniform distribution of metal cations in the laminae, exchange of intercalated anions, visible light response, and strong alkalinity and adsorption, they have attracted increasing attention in the field of photocatalysis [19–22]. Ye et al. [23] synthesized catalyst Ce-LDH, which achieved a CO production rate of 1.68 $\mu\text{mol}\cdot\text{g}^{-1}\cdot\text{h}^{-1}$ under simulated sunlight irradiation without any sacrificial agent or noble metals. Although LDHs show great potential in the photocatalytic reduction of CO₂, their photocatalytic activity is limited by the rapid recombination of photoinduced carriers. 2D g-C₃N₄ (CN) nanosheets are metal-free polymer semiconductors that have been extensively studied

* Corresponding authors.

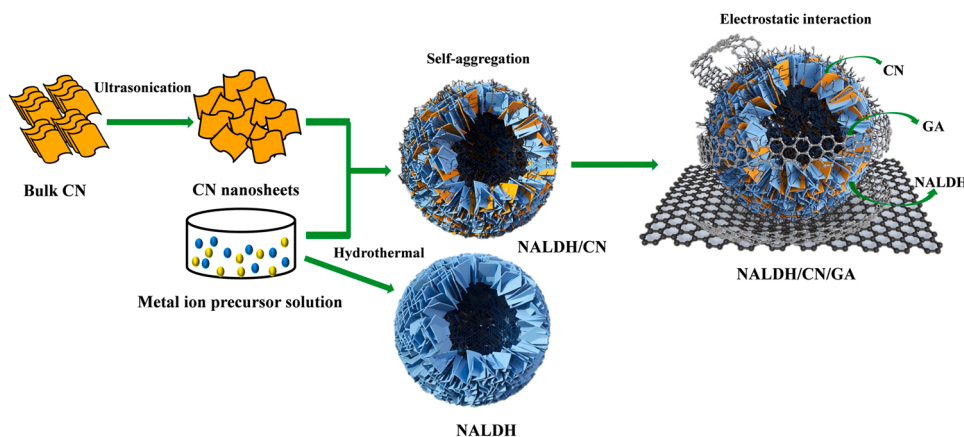
E-mail addresses: Jdyoujili@vip.163.com (Y. Li), Chemtangjsu@163.com (S. Tang), Linxiao2017@whu.edu.cn (X. Lin), Chenfeitai@163.com (F. Chen).

<https://doi.org/10.1016/j.apcatb.2022.121065>

Received 25 November 2021; Received in revised form 27 December 2021; Accepted 2 January 2022

Available online 21 January 2022

0926-3373/© 2022 Elsevier B.V. All rights reserved.



Scheme 1. Synthetic process for NALDH/CN/GA hybrid.

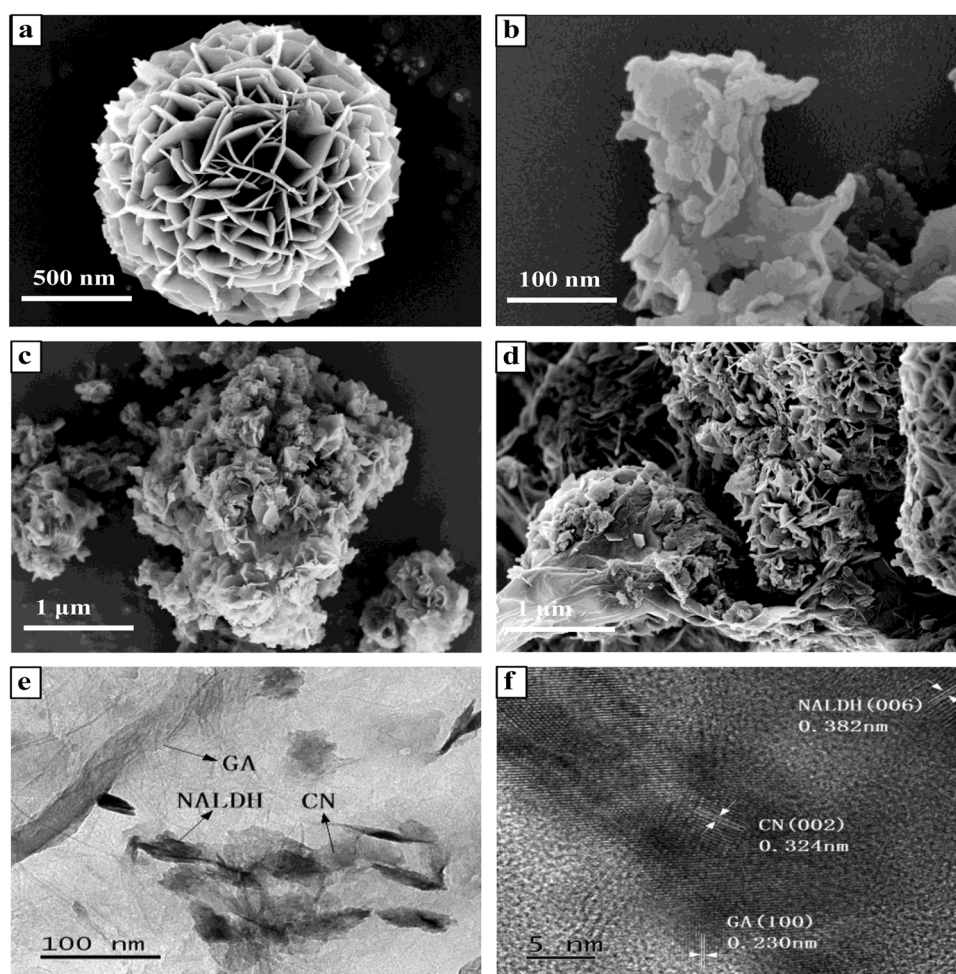


Fig. 1. SEM images of (a) NALDH, (b) CN, (c) NALDH/CN, and (d) NALDH/CN/GA-20; TEM image of (e) NALDH/CN/GA-20; and (f) HRTEM image of NALDH/CN/GA-20.

in photocatalytic CO_2 reduction owing to their chemical stability, low cost, non-toxicity, adjustable electronic structure, and suitable CO_2 reduction potential [24–27]. However, they exhibit unsatisfactory CO_2 reduction owing to defects, low solar energy utilization, and rapid recombination of photoinduced carriers [28]. LDH/CN 2D–2D heterojunction composites can greatly reduce the recombination of electron–hole pairs and improve the optical response to visible light [29–31]. Composite heterojunction with intimate interface contact could shorten

the charge migration distance and then efficiently accelerate the transfer and separation of photo-induced charge carriers. Recently, Zhao et al. [32] prepared NiFe-LDH/g-CN composites for CO_2 reduction, achieving a highest CO production rate of $13.95 \mu\text{mol} \cdot \text{g}^{-1} \cdot \text{h}^{-1}$ and CO selectivity of 73.2%. To further improve the separation of electron–hole pairs and high surface area of nanocomposite photocatalysts, graphene aerogel (GA) with a three-dimensional (3D) structure is an ideal support and charge carrier shuttle owing to its excellent electrical conductivity and

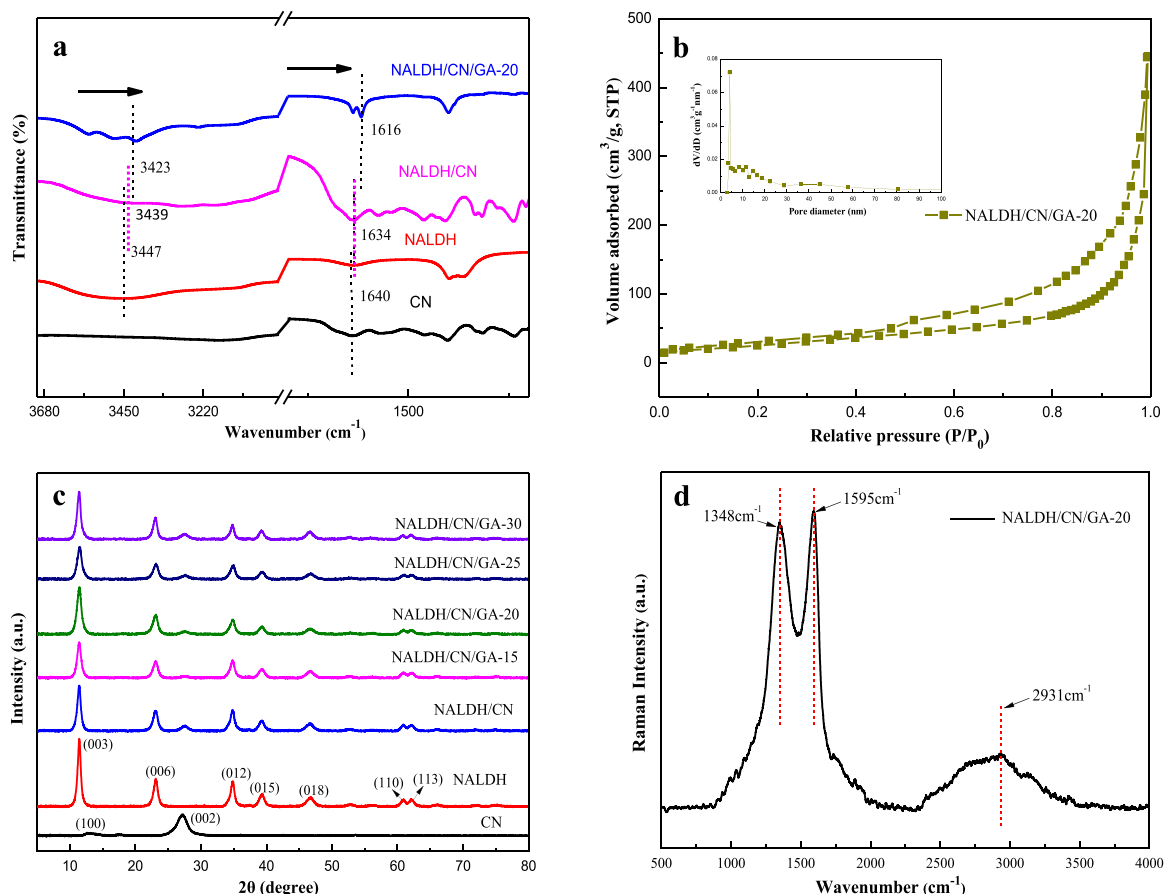


Fig. 2. (a) The FT-IR spectra, (b) N₂ adsorption-desorption isotherms and corresponding pore size distribution profiles (the inset), (c) XRD patterns of synthesized samples, (d) Raman spectra of as-prepared NALDH/CN/GA-20.

Table 1

BET surface areas and pore parameters of samples.

Samples	S _{BET} (m ² ·g ⁻¹)	Average pore size (nm)	Total pore volume (cm ³ ·g ⁻¹)
CN	42	24.12	0.251
NALDH	74	28.19	0.520
NALDH/CN	84	27.03	0.689
NALDH/CN/GA-20	102	42.02	0.878

flexibility, and large specific surface area. Wan and coworkers [33] prepared a C₃N₄/GO aerogel mixture with a macroscopic three-dimensional (3D) structure using a one-step cryodesiccation method, which exhibited strong visible light catalytic performance in dye degradation. Yang et al. [34] constructed an urchin-like CoZnAl-LDH/RGR/g-C₃N₄ photocatalyst with a Z-scheme charge flow mode, which promoted photoinduced carrier separation. The CO production rate reached 10.11 μmol·g⁻¹·h⁻¹ and the CO selectivity was above 96%. This performance was attributed to the well-defined flexible 3D architecture. The highly porous and conductive network provided abundant channels for efficient electron transfer and hole diffusion. However, to date, 3D aerogel-based 2D–2D hybrid heterojunctions for photocatalytic CO₂ conversion have rarely been reported.

Accordingly, in this study, a NiAl-LDH/g-C₃N₄/GA hybrid heterojunction system was constructed using a facile hydrothermal method. Under visible light, CO₂ was effectively reduced to CO in water vapor using a single integrated system utilizing sunlight, which is the ultimate goal of artificial photosynthesis. The high specific surface area, visible light absorption capacity, low photoinduced carrier recombination, and

rapid charge transfer observed in the mixed system resulted in improved CO₂ reduction performance. To our knowledge, this represents the first successful synthesis of NiAl-LDH/g-C₃N₄/GA with a 3D aerogel-based 2D–2D hybrid heterojunction for efficient CO₂ reduction under visible light (Scheme 1).

2. Experimental

2.1. The synthesis of NALDH/CN/GA

Scheme 1 shows the fabrication process of the NALDH/CN/GA hybrid system using a facile hydrothermal method. The g-C₃N₄ nanosheets were synthesized by simple thermal treatment of urea. Briefly, urea powder (6 g) was placed in a covered alumina crucible and thermally treated at 550 °C for 4 h in a quartz tube furnace with a heating rate of 2 °C/min under a nitrogen atmosphere, denoted as CN. The 2D flower-like pure NiAl-LDH nanosheets, denoted as NALDH, were prepared by urea decomposition with NH₄F as a form control agent [35]. NALDH/CN with various CN contents were synthesized in situ by coprecipitation of NALDH onto the prepared CN nanosheets in a facile hydrothermal process. GA (0.03 g) was dispersed in DI water (16 mL) by sonication for 1 h, and NALDH/CN was added, followed by vigorous stirring for 18 h. The product was then freeze-dried and ground, denoted as NALDH/CN/GA. For comparison, pure NALDH without CN and GA added, and NALDH/CN without GA added, were synthesized using the same procedure. More details are shown in Section 1.1 of Supporting information, and the characterizations of photocatalyst were illustrated in Section 1.2 of Supporting information.

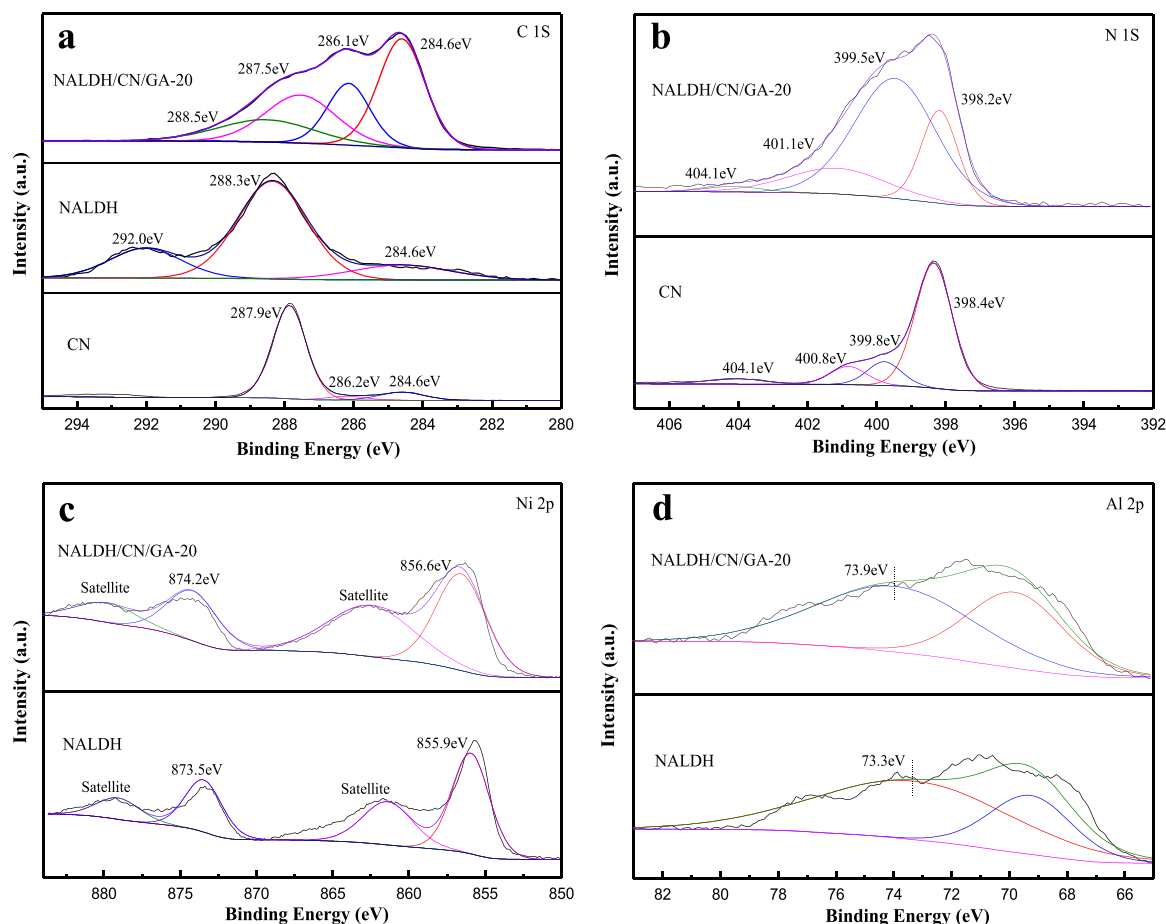


Fig. 3. (a) C 1 s, (b) N 1 s, (c) Ni 2p, and (d) Al 2p high-resolution XPS spectra.

2.2. Evaluation of photocatalytic activity

Photocatalytic CO₂ reduction was conducted in a gas-closed circulation system using a 300-W Xenon lamp equipped with a 420-nm cut off filter as the light source. The sample (10 mg) was evenly dispersed on a round glass with a diameter of 4 cm. DI water (5 mL) was injected into the reactor, and filled with 0.2 bar CO₂ (99.999%). Finally, the products were quantitatively analyzed by gas chromatography (GC-7920, Beijing, China). More details are shown in Section 1.4 of Supporting information.

3. Results and discussion

3.1. Ultratight sheet-sheet heterojunctions induced via steric effect and hydrogen bonding

In order to analyze formation of sheet-sheet heterojunctions induced via steric effect and hydrogen bonding, the morphologies and microstructures of some representative samples were characterized by SEM and TEM. As shown in Fig. 1a and b, Pure NALDH was consisted of large-interface and 2D (two-dimensional) nanosheets with a wideness and thickness about 50 nm and 0.8 nm, respectively [36]. 2D nanosheets interweaved into a flower-like network framework induced via steric effect and hydrogen bonding of the layered double hydroxides [22]. Pure CN possessed a 2D sheet-like structure with irregular orientation. By ultrasonication, CN was stripped into small-sized nanosheets, and numerous segregated 2D NALDH nanosheets were in intimate contact with the 2D CN nanosheets (Fig. 1c). Subsequently, during hydrothermal treatment, a large number of ultratight sheet-sheet heterojunctions with coupling large interfaces were synthesized and assembled into network frameworks in NALDH/CN due to steric effect and hydrogen

bonding of double nanosheets containing hydroxides and nitrogen hydrides. It shorts the charge transmission distance, thereby facilitating the transfer and separation of photo-induced charge carriers, reactant adsorption and mass transport. By introduction of GA, the interfacial interaction between NALDH nanosheets and CN nanosheets was more strong due to graphene entwining with a curly folded layer structure (Fig. 1d and e), which was supported by more HRSEM images (Figs. S1a-c). NALDH/CN/GA remains network morphology, which indicates that steric effect and hydrogen bonding may play a vital role in the self-assembly process. It could efficiently accelerate rapid charge transfer and light absorption. Lattice fringes with interlayer distances of 0.324, 0.382, and 0.230 nm were observed in the HRTEM image (Fig. 1f), corresponding to the (002) plane of CN, (006) plane of NALDH, and (100) plane of GA, respectively [34,37].

Moreover, the EDS elemental mapping image for NALDH/CN/GA-20 shows the well distributed C, N, O, Ni and Al elements (Fig. S2), which demonstrates that NiAl-LDH, GA and g-C₃N₄ jointly contributed to the formation of the network framework with ultratight sheet-sheet heterojunctions. Additionally, the Ni/Al molar ratio was approximately 3 as shown in EDS elemental spectrum (Fig. S2), which is close to the theoretical value for pristine NALDH, and indicated the formation of abundant coupling interfaces in ultratight sheet-sheet heterojunctions. The content of NiAl-LDH, GA and g-C₃N₄ in the NALDH/CN/GA-20 composite was further determined by thermogravimetric (TG) analysis (Fig. S3). The actual content of NiAl-LDH, GA and g-C₃N₄ in NALDH/CN/GA-20 can be determined as 40 wt%, 37 wt% and 23 wt% respectively. It was consistent with EDS elemental spectrum analysis (Fig. S2). Hydrogen bonding acts a pivotal part in a facile hydrothermal process of NALDH/CN/GA. Hence, infrared (IR) spectroscopy was employed to verify the hydrogen bonding interaction of the ultratight sheet-sheet

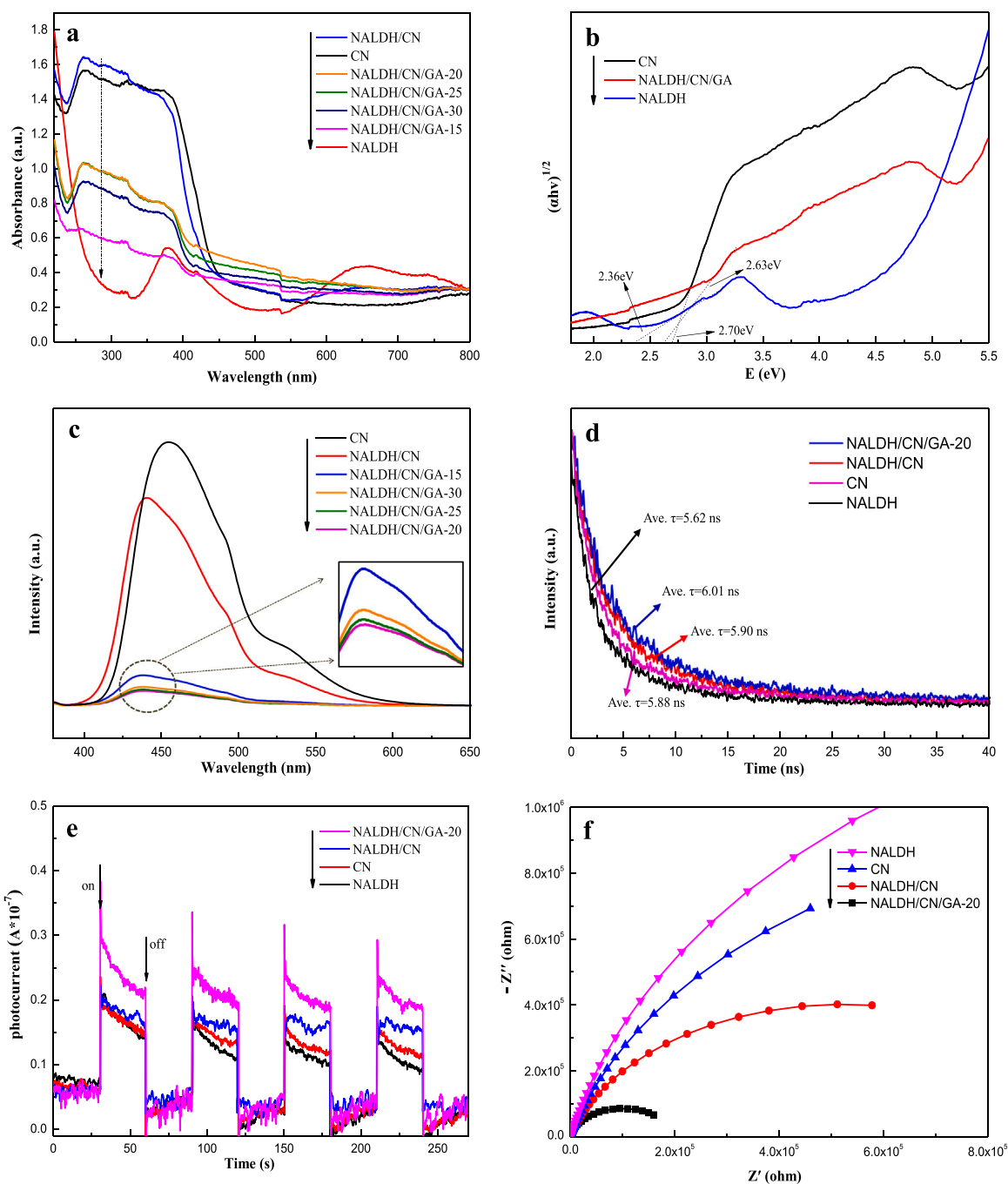


Fig. 4. (a) UV-vis diffuse reflectance spectra; (b) band gaps; (c) PL spectra (excitation wavelength, 370 nm); (d) time-resolved fluorescence decay traces; (e) transient photocurrent responses and (f) electrochemical impedance spectra of the as-prepared samples.

heterojunctions in NALDH/CN/GA. NALDH/CN/GA-20 shows a series of peaks in the region of $600\text{--}3700\text{ cm}^{-1}$, assigned to C—N, N—H, O—H, M—O—M and M—OH characteristic peaks (Fig. S4). As shown in Fig. 2a, the -OH of the interlayer water molecules in NALDH and -NH of uncondensed amino groups in CN exist intermolecular hydrogen bonds. Since the hydrogen bond is formed, the electron cloud density is averaged and the molecular energy decreases, then the vibration frequency shifts to a lower wavenumber in IR [38]. As shown in Fig. 2a, the peak location of OH stretching vibration in NALDH/CN/GA (3423 and 1616 cm^{-1}) moves to a lower wavenumber, compared with NALDH/CN (3439 and 1634 cm^{-1}). The IR results indicate that NALDH/CN/GA has a relatively strong hydrogen bonding interaction, which contributes to constructs ultratight sheet-sheet heterojunctions with short-range

coupling interfaces. Additionally, in comparison with CN, the C—N signal at 1240 cm^{-1} of NALDH/CN/GA was weak due to the intermolecular hydrogen bonds between CN and NALDH. It also confirmed successful synthesis of the ultratight sheet-sheet heterojunctions in NALDH/CN/GA. Fig. 2b shows the N_2 adsorption-desorption isotherms and the BJH pore-size distribution curves of the NALDH/CN/GA-20 with pore size distribution ranged from 10 to 30 nm, which may be due to the integration of nanosheets leading to the formation of mainly mesoporous structures by steric effect and hydrogen bonding [39,40]. Other catalysts also showed type-IV isotherm and H3 hysteresis loops with the existence of porous structure (Fig. S5). The BET results illustrate that ultratight sheet-sheet heterojunctions can be self-assembled into network structures with significantly different specific surface area and

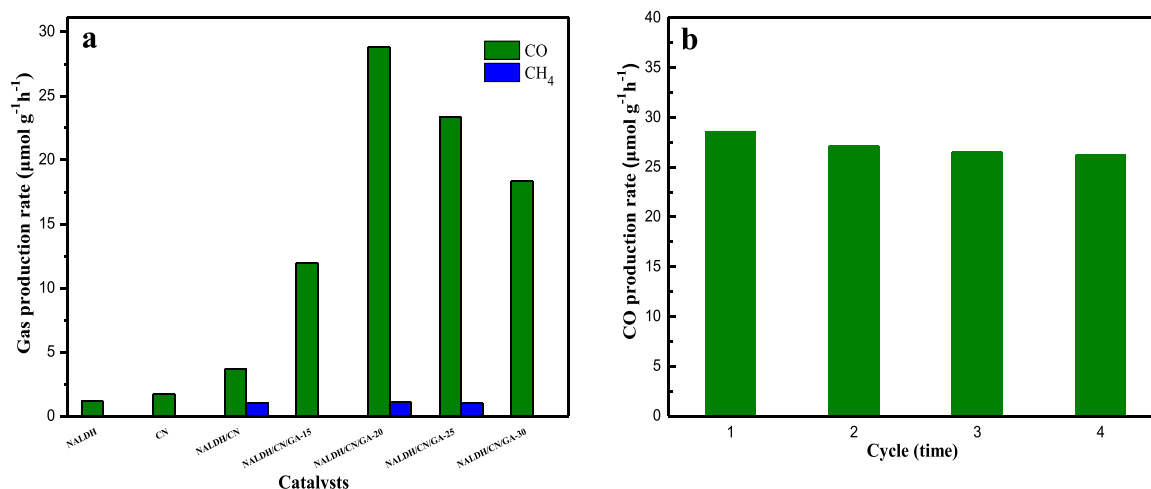


Fig. 5. (a) CO and CH₄ average gas production rates over all synthesized photocatalysts, (b) recycling test of photocatalytic CO production rate over NALDH/CN/GA-20.

Table 2

Comparison of photocatalytic CO₂ reduction activities for photocatalysts in this work and those reported in the literature.

Photocatalyst	Reducing agent	Light source	CO production (μmol·g ⁻¹ ·h ⁻¹)	Ref
CoSe ₂ /C ₃ N ₄ /GA	3 mL water	300 W Xe	5.75	[63]
P25@CoAl-LDH	5 mL water	300 W Xe	2.21	[45]
ZnM-LDHs (M = Ga, Al)	0.1 mL water	300 W Xe	1.6 (Al), 1.3 (Ga)	[64]
GDY@CNTb	0.1 mL water	300 W Xe	7.33	[65]
CoZnAl-LDH/ RGO/g-C ₃ N ₄	0.4 mL water	300 W Xe	10.11	[34]
ZnAl-LDH	water vapor	300 W Xe	7.6	[66]
NiFe-LDH/g-C ₃ N ₄	19 mL water	300 W Xe	13.95	[32]
CdS/CdWO ₄	water vapor	300 W Xe	1.4	[67]
CdS/Ni-MOF	water vapor	300 W Xe	1.87	[68]
SnS ₂ atomic layers	5 mL water	300 W Xe	12.28	[69]
FeOOH/CdS	5 mL water	300 W Xe	12.55	[70]
β-In ₂ S ₃ /NDCN	20 mL water	300 W Xe	20.32	[71]
NALDH/CN/GA	Water vapour	300 W Xe	28.83	This work

pore volume (Table 1).

XRD patterns were performed in order to characterize the crystal structure variation of as-prepared samples in formation of sheet-sheet heterojunctions. As shown in Fig. 2c, pure CN has two diffraction peaks at about 13.2° and 27.4°, attributed to the (100) and (002) planes, respectively, which reflect the in plane structural repeating unit and inter-layer stacking of a conjugated aromatic system, consistent with the pattern reported for this material (JCPDS 87-1526) [41,42]. The diffraction peaks of NALDH were consistent with those of the standard hydrotalcite-like LDH (JCPDS 15-0087), with typical peaks located at 2θ values of 11.48° (003), 23.16° (006), 34.91° (012), 39.36° (015), 46.79° (018), 60.01° (110), and 62.15° (113), confirming the successful synthesis of NALDH [43]. The diffraction peak of the NALDH phase was observed at 0.77 nm (d₀₀₃), indicating the presence of interlayer CO₃²⁻ [44]. NALDH/CN/GA hybrid systems with different CN contents had

similar diffraction patterns to that of pristine NALDH. Meanwhile, the diffraction peak at 27.4° obviously became stronger with increasing CN content, thus indicating the existence of g-C₃N₄. Moreover, the (003) diffraction peak for all NALDH/CN/GA gradually shifts to a low angle in compared to NALDH, which demonstrates that some g-C₃N₄ and GA may intercalate into the interlayer of NiAl-LDH nanosheets. The deviation of (003) peak of the XRD patterns can be further confirmed from its zoomed view (Fig. S6). Indeed, such a phenomenon also has been well documented in previous works concerning the modification of NALDHs [36,38]. However, the diffraction peaks of GA were not observed in the hybrid, perhaps due to being shielded by the main peak [45]. Raman spectroscopy was conducted to further confirm the presence of GA. the G-band (1595 cm⁻¹) and D-band (1348 cm⁻¹) are associated with graphitic carbon, and structural defects or partially disordered graphitic domains (Fig. 2d), respectively. Furthermore, the signal at 2931 cm⁻¹ was due to combination of the D and G bands in the first-order spectrum, which was caused by lattice disorder [46,47]. All results confirmed the successful synthesis of NALDH/CN/GA with ultratight sheet-sheet heterojunctions.

XPS was used to investigate the chemical states for the surface elements of catalysts. The survey spectra in Fig. S7 affirm that NALDH/CN/GA consist mainly of C, N, Ni, Al, and O, confirming the presence of CN and NALDH in the hybrid system, which corresponded to the results obtained by EDS analysis. As shown in Fig. 3a, the C 1s spectrum of CN was deconvoluted into three peaks located at binding energies of 284.6, 286.2, and 287.9 eV, attributed to C-C/C=C, C-NH₂, and N-C=N, respectively. For NALDH, the C 1s peaks were associated with carbon contamination (284.6 eV), C-O (288.3 eV), and C=O (292.0 eV) due to presence of large amounts of carbonate [48,49]. For NALDH/CN/GA, adventitious and graphitic carbon (284.6 eV), C-NH₂ (286.1 eV), C-O (287.5 eV), and N-C=N (288.5 eV) peaks were observed in the C 1s spectrum, and disappearance of the peak at 292.0 eV was attributed to carbonate being replaced by intercalated CN and GA. This further confirmed that there existed strong interfacial interaction between 2D NiAl-LDH and 2D g-C₃N₄ in sheet-sheet heterojunctions. Additionally, the binding energies of carbon species were different to those in CN or NALDH, also demonstrating the strong chemical interactions among NALDH, CN, and GA, which facilitated charge separation. The N1s fine spectrum of pure CN (Fig. 3b) was fitted by four peaks located at binding energies of 398.4, 399.8, 400.8, and 404.1 eV, which were assigned to nitrogen-bonded species C-N=C, N-(C)₃, C-NH₂, and C-N-H, respectively, which were consistent with NALDH/CN/GA [50,51]. Fig. 3c shows the Ni 2p fine spectra. For pure NALDH, the binding energies at 855.9 and 873.5 eV were assigned to Ni 2p_{3/2} and Ni 2p_{1/2}, respectively,

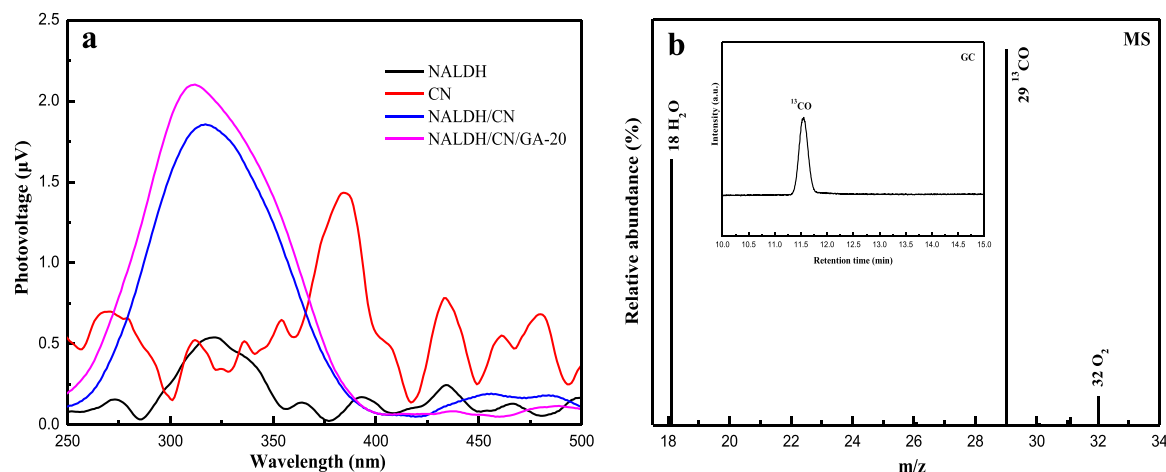


Fig. 6. Surface photovoltage of catalysts GC–MS analysis of carbon isotope (^{13}C) labeling experiment using NALDH/CN/GA-20 as catalyst.

in agreement with the Ni^{2+} oxidation state, and the additional satellite peaks indicated that Ni in NALDH was in the high-spin divalent valence state [52]. Meanwhile, an obvious increase in the binding energies of Ni $2p_{3/2}$ and Ni $2p_{1/2}$ was observed in NALDH/CN/GA. Furthermore, the Al $2p$ spectra (Fig. 3d) of NALDH showed a typical peak at 73.3 eV, corresponding to the Al^{3+} oxidation state, while NALDH/CN/GA showed the Al $2p$ peak at 73.9 eV [53,54]. These changes in binding energy indicated strong interfacial interactions between different components. The positive shift of binding energy for Ni $2p$ and Al $2p$ components, and negative shift of binding energy for N1s, might be due to strong electron transfer between NALDH and CN, which leads to decreased or increased electron density on the surface of materials [30]. Interface interaction is conducive to the rapid migration and separation of charges, which improve the CO_2 reduction performance.

3.2. Charge separation and transfer promoted via ultratight sheet-sheet heterojunctions

To elucidate the effects of ultratight sheet-sheet heterojunctions on optical properties and photoexcitation charge separation, photoelectrochemical characterizations were performed. As shown in Fig. 4a, NALDH showed intrinsic optical absorption bands in both the UV and visible light regions, with the intrinsic absorption band in the UV region (200–300 nm) corresponding to ligand-to-metal charge transfer (LMCT) from the O $2p$ orbital to the Ni $3d\ t_{2g}$ orbital, while those in the visible light region were related to d–d transitions [29,55]. Furthermore, the bands at 420 and 652 nm were attributed to spin-forbidden transitions $^3A_{2g}(\text{F}) \rightarrow ^1T_{2g}(\text{D})$ and $^3A_{2g}(\text{F}) \rightarrow ^1E_g(\text{D})$, respectively. The other bands, located at 380 and 740 nm, were assigned to spin-allowed transitions $^3A_{2g}(\text{F}) \rightarrow ^3T_{1g}(\text{P})$ and $^3A_{2g}(\text{F}) \rightarrow ^3T_{1g}(\text{F})$, which resulted from the d^8 configuration of Ni^{2+} ions in an octahedral field [55,56]. Simultaneously, pure CN showed the strong UV absorption in comparing to visible absorption. Compared with NALDH, NALDH/CN and NALDH/CN/GA showed blue-shifted absorption edges owing to the presence of CN with the aforementioned characteristic UV-region absorption bands. However, both photocatalysts possessed no typical absorption bands of NALDH, which were attributed to the strong interaction between CN and NALDH via steric effect and hydrogen bonding. After introduction GA, the presence of carbon led to an upward shift of the visible absorption spectrum in compared to CN [57,58]. The bandgap energies of the samples were estimated from the plots in Fig. 4b using the Kubelka–Munk function. The bandgap energies (E_g) of NALDH, CN, and NALDH/CN/GA-20 were determined to be approx. 2.36, 2.70, and 2.63 eV, respectively. Therefore, the UV–DRS results suggested that the Z-scheme transfer route was not suitable for the NALDH/CN/GA-20 hybrid system, of which E_g is less than that of CN.

Compared with CN, the PL emission intensities of NALDH/CN were lower (Fig. 4c), which was attributed to the formation of ultratight sheet-sheet heterojunctions between NALDH and CN with the shortened charge transmission distance, thereby weakening the recombination of photogenerated electron–hole pairs. By introduction of GA, interfacial interaction between NALDH nanosheets and CN nanosheets was more strong, which could efficiently accelerate the transfer and separation of photo-induced charge carriers in the ultratight sheet-sheet heterojunctions, resulting in NALDH/CN/GA-20 showed the lowest PL emission intensity. Additionally, the NALDH/CN and NALDH/CN/GA photocatalysts exhibited a blue shift compared with CN, which was attributed to the differently intrinsic electronic structures of CN [59,60]. This also indicated the strong hybridized interaction between NALDH and CN, which formed sheet-dependent contact heterojunctions entwined with GA. To further elucidate the effect of ultratight sheet-sheet heterojunctions on photoexcitation charge separation of NALDH/CN/GA composites, especially NALDH/CN/GA-20, photoelectrochemical characterizations were performed. The charge transfer dynamics for representative samples were investigated by time-resolved photoluminescence (TRPL) decay spectra (Fig. 4d). Evidently, the average lifetime of the photogenerated charge carries in NALDH/CN/GA-20 (6.01 ns) is more prolonged than that of other samples, of which average lifetime was obtained by substituting the data A1, A2, T1 and T2 in the table into the formula (Table S1). It is well-known that a longer lifetime of electrons and holes implies a high probability for participation in photocatalytic reaction and improved activity [61]. Simultaneously, the NALDH/CN/GA-20 catalyst exhibited the highest photocurrent response after several periods of intermittent irradiation (Fig. 4e) and the smallest arc diameter (Fig. 4f). This was attributed to the ultratight sheet-sheet heterojunctions entwined with GA, which could efficiently accelerate the transfer, separation of photo-induced charge carriers, and enhanced light absorption performance [62].

3.3. Enhanced photocatalytic performance via ultratight sheet-sheet heterojunctions and mechanism of CO_2 reduction

The photocatalytic CO_2 reduction activity of the as-prepared samples was investigated under visible light irradiation. The control experiments were conducted in the absence of light or catalyst, with the results showing that no reduction product was detected, indicating that light and catalyst were essential for the CO_2 photocatalytic reduction process. The main product was CO, while only a small amount of CH_4 was detected during the reaction. As shown in Fig. 5a, pure CN and NALDH exhibited poor CO production, the CO production rate of 1.21 and 1.82 $\mu\text{mol}\cdot\text{g}^{-1}\cdot\text{h}^{-1}$, respectively. The photocatalytic activity of NALDH/CN

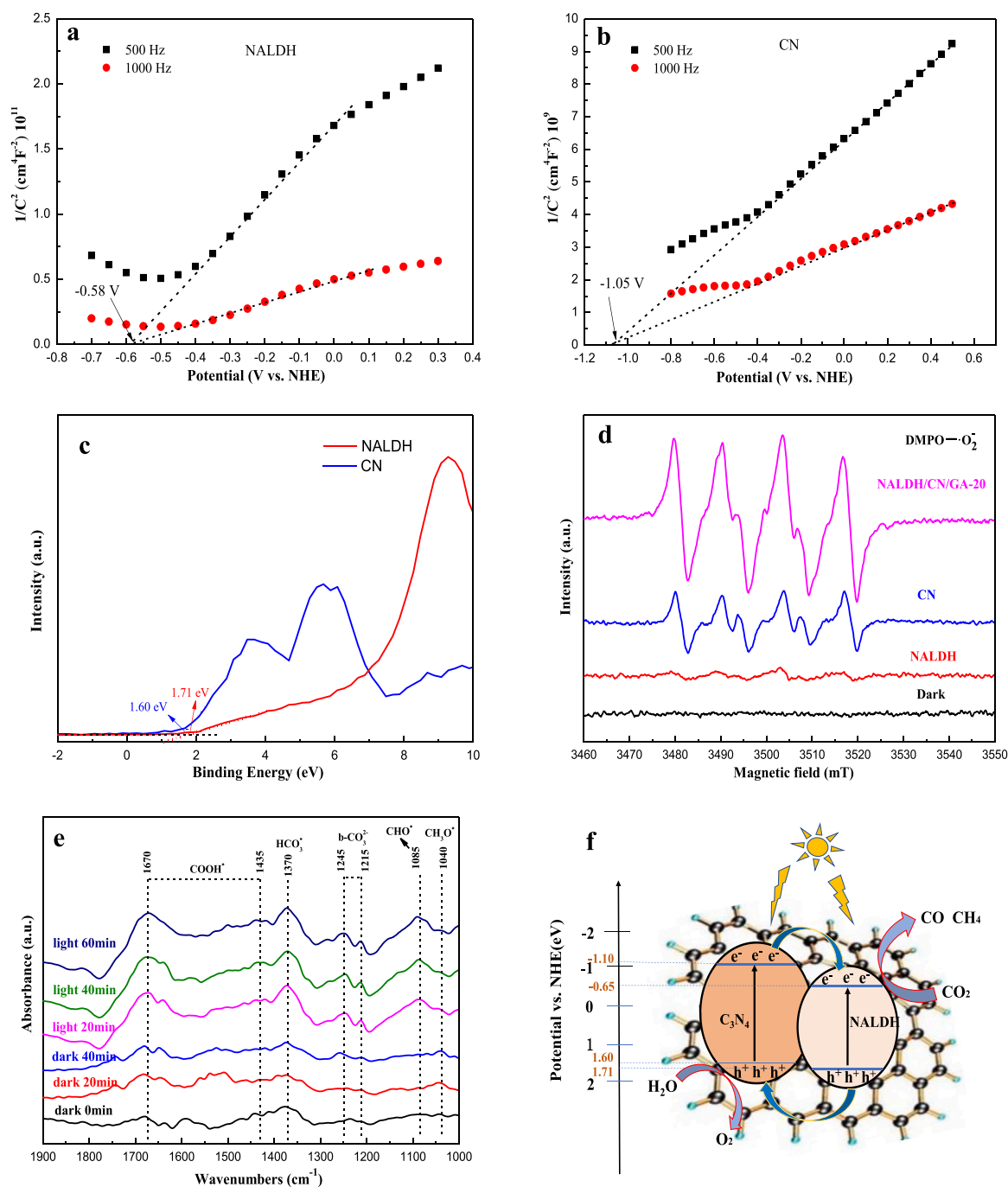


Fig. 7. Mott-Schottky plots of (a) NALDH and (b) CN samples, valence band XPS spectra of (c) NALDH and CN samples, (d) DMPO spin-trapping ESR spectra of different samples for $\text{DMPO} \cdot \text{O}_2^-$ irradiated for 6 min, (e) *In-situ* ISFT-IR spectra of NALDH/CN/GA-20, and (f) schematic diagram of possible photocatalytic mechanism for NALDH/CN/GA.

was clearly improved compared with that of pure CN and NALDH, with CO production rate of $3.71 \mu\text{mol} \cdot \text{g}^{-1} \cdot \text{h}^{-1}$. This might be attributed to the formation of ultratight sheet-sheet heterojunctions between NALDH and CN, which can decrease photoinduced charge recombination. Furthermore, with the introduction of GA, the effect of ultratight sheet-sheet heterojunctions on photocatalytic activity of the hybrid system was significantly improved. For NALDH/CN/GA-20, the CO yield rate reached $28.83 \mu\text{mol} \cdot \text{g}^{-1} \cdot \text{h}^{-1}$, which was 24, 16 and 8 times those of pure NALDH, CN and NALDH/CN, respectively. The introduction of GA as an electronic medium and entwining agent, could furthermore promote charge transfer and coupling interface adhesion of heterojunctions, which enhance the separation of electron-hole pairs and mass

transport. Additionally, GA, CN/GA, NALDH/GA, NALDH/CN achieved CO yield of 0.26, 2.30, 1.70 and $18.53 \mu\text{mol} \cdot \text{g}^{-1}$ under five hours of visible light irradiation, respectively (Fig. S8). Obviously, photocatalytic CO_2 reduction performance of NALDH/CN was higher than that of CN/GA and NALDH/GA. It illustrated ultratight sheet-sheet heterojunctions showed more important effects on photocatalytic CO_2 reduction of NALDH/CN/GA than GA. With increasing CN content, the CO production rate of the NALDH/CN/GA hybrid increased, with the maximum value of $28.83 \mu\text{mol} \cdot \text{g}^{-1} \cdot \text{h}^{-1}$ CO obtained by NALDH/CN/GA-20. When the CN content exceeded 20%, the CO production rate decreased, which might be due to the stacking of CN nanosheets. This would lead to the material structure collapsing and the surface active sites being covered.

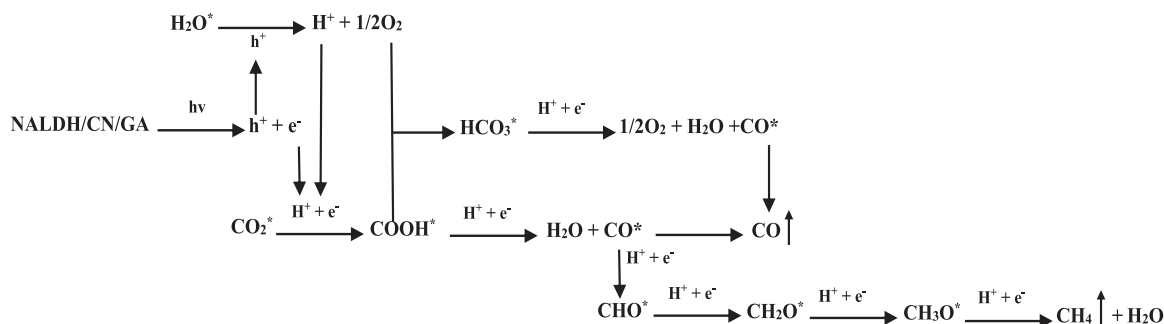


Fig. 8. The possible pathways of the CO₂ photocatalytic reduction, where * indicates the adsorbed state.

The photocatalytic CO₂ reduction efficiency of NALDH/CN/GA with different CN content was consistent with the PL emission peak strength (Fig. 4c). Notably, the photocatalytic activity of the NALDH/CN/GA-20 was higher than that of previously reported catalysts, of which was applied to conventional CO₂ photocatalytic reduction by only using water as reducing agent, as shown in Table 2. Additionally, compares the overall CO and CH₄ evolution rates of all prepared samples. Only NALDH/CN, NALDH/CN/GA-20, and NALDH/CN/GA-25 were produced very small amounts of CH₄. It was probably attributed to the more suitable E_{CB} level of above three samples than other composites, because the conversion of CO₂ to CH₄ and CO need much differently negative potential (ECO₂/CH₄ = −0.24 V vs. NHE, E CO₂/CO = −0.53 V vs. NHE). As shown in Fig. 5b, the activity of NALDH/CN/GA-20 did not clearly decrease, with 91–95% of the original photocatalytic activity remaining after four recycles with more than 100 repeating experiments, confirming favorable photostability. It was attributed to hybrid system with high structural stability and strong interfacial interactions of ultratight sheet-sheet heterojunctions, as a consequence of the FT-IR spectra without obvious differences for the catalyst before and after use (Fig. S9).

The surface photo-voltage spectra was used to further explore photo-generated carrier separation efficiency (Fig. 6a). Compared with SPV signal of NALDH and CN, the signal of NALDH/CN and NALDH/CN/GA-20 was significantly improved. The NALDH/CN/GA-20 has the strongest SPV signal. It may be due to ultratight sheet-sheet heterojunctions between NALDH and CN entwined with GA, which enhanced strong interfacial interaction of heterojunctions by its curly folded layer structure. Thus the catalyst enhances the photogenerated electron capture ability and decreases the photogenerated carrier recombination rate, thus increasing the utilization rate of photogenerated electrons and enhancing the photocatalytic performance [72,73]. To verify that the generation of carbon-based CO or CH₄ was not due to organic residues, Ar was used instead of CO₂ under the same experimental conditions. No CH₄ or CO production was detected after 5 h of light irradiation, indicating that the carbon source was CO₂. Additionally, A ¹³CO₂ isotope labeling experiment (Fig. 6b) was performed using NALDH/CN/GA-20 as catalyst. The peak detected by GC (inset of Fig. 6b) with a signal at *m/z* 29 in the MS spectrum was attributed to ¹³CO, which showed that the CO product originated from CO₂. In order to elucidate the mechanism of accelerating the separation of charge pairs, we accurately analyzed the semiconductor type, donor density and energy band position of catalysts by the Mott-Schottky method and valence band XPS (VB-XPS). Fig. 7a and b show the Mott-Schottky plots of NALDH and CN catalysts, and the positive slope of NALDH and CN were indicated the n-type semiconductor. The slightly enhanced slope values for NALDH imply the increased donor density compared with CN [74]. More specifically, the flat-band potentials of NALDH (−0.58 V vs. NHE) and CN (−1.05 V vs. NHE) were obtained by extrapolating the Mott-Schottky plots in Fig. 7a and b. The flat-band potentials of NALDH and CN were obvious the relatively negative CB potential compared with that of CO₂/CO (−0.53 eV vs. NHE), CB electrons in the NALDH and CN can

directly reduce CO₂ to CO. To determine the exact CB and VB positions for each component, VB-XPS analysis were measured as shown in Fig. 7c. Herein, the VB edge potentials of NALDH and CN, determined from the intercepts of tangents to the density of states at the Fermi edge, were 1.71 and 1.60 eV, respectively. Based on the band gap energies of NALDH (2.36 eV) and CN (2.70 eV) that were determined in the UV-DRS analysis, the corresponding CB edge potentials were calculated to be −0.66 eV and −1.10 eV, respectively. Both the CB and VB potentials of NALDH were more positive than those of CN. The band structure of NiAl-LDH and g-C₃N₄ was further determined by ESR analysis for an investigation of the transfer path of light-induced electrons and holes. Fig. 7d showed six characteristic peaks of the DMPO-•O₂[−] adduct. Compared with CN and NALDH, the DMPO-•O₂[−] signal intensity of NALDH/CN/GA-20 was significantly increased, which might be due to the transfer of photoinduced electrons from the conduction band (CB) of CN to the CB of NALDH [51]. More importantly, the no characteristic peaks of the DMPO-•OH adduct was observed for NALDH/CN/GA-20, NALDH and CN as shown in Fig. S10, which was in accordance with the potential of its valence band (VB). No ESR signals were detected in the catalysts under dark conditions, which indicated that the spin-reactive species were produced under light irradiation [75]. To investigate groups formed on the catalyst surface during the photocatalytic CO₂ reduction reaction, and predict the intermediates, in-situ FT-IR (ISFT-IR) spectroscopy experiments were conducted on the NALDH/CN/GA-20 catalyst. As shown in Fig. 7e, multiple intermediate products, including HCO₃[−] (1370 cm^{−1}), b-CO₃^{2−} (1245 and 1215 cm^{−1}), CHO* (1085 cm^{−1}), CH₃O* (1040 cm^{−1}), and COOH* (1670 and 1435 cm^{−1}) were observed [70,76–78]. Notably, the concentration of COOH* and CH₃O* intermediates increased significantly under light irradiation, suggesting that COOH* and CH₃O* were the main intermediates of the CO₂ reduction process [77,79]. By integrating the results above, based on type-II NALDH/CN/GA hybrid system (Fig. 7f), the multi electron series reduction mechanism was proposed to explain the CO₂ reduction pathway as shown in Fig. 8. Upon the visible light irradiation, the electrons on the valence band (VB) of CN and NALDH can be excited into the conduction band (CB). Meanwhile, the formed holes on the VB of NALDH transfer into the VB of CN, and the electrons transfer from the CB of CN to the CB of NALDH. Subsequently, compared with that of CO₂/CO (−0.53 eV vs. NHE), owing to the relatively negative CB potential (−0.68 eV vs. NHE) and the flat-band potential (−0.58 V vs. NHE) of NALDH, electrons in the NALDH CB can directly reduce CO₂ to CO via HCO₃[−] and COOH* intermediates with the multi electron series reduction process [54,79,80]. And the detailed CO₂ reduction process is conducted by a series of equations in the Table S2.

4. Conclusions

A new type of NALDH/CN/GA hybrid system with aerogel-based ultratight sheet-sheet heterojunctions, was successfully designed for CO₂ reduction. Notably, the NALDH/CN/GA-20 hybrid system showed a

remarkable CO production rate of $28.83 \mu\text{mol}\cdot\text{g}^{-1}\cdot\text{h}^{-1}$, which was 24 and 16 times those of pure NALDH and bare CN, respectively. Furthermore, it was far exceeding the reported conventional CO₂ photocatalytic reduction efficiency. Meanwhile, this NALDH/CN/GA-20 hybrid system exhibited exceptional stability. A corresponding photocatalytic mechanism about the multi electron series CO₂ reduction process was proposed. This well-designed approach might pave the way for the preparation of other hybrid systems with high photocatalytic activity, and further utilization in environmental science and energy.

CCRediT authorship contribution statement

Min Yang: Experimental, Conceptualization, Methodology, Formal analysis, Data curation, Validation, Resources, Writing – original draft, Writing – review and editing. **Peng Wang:** Experimental, Data curation, Validation. **Xiao Lin:** Writing – original draft, Writing – review and editing. **Youji Li:** Supervision, Project administration, Funding acquisition, Writing – review and editing. **Senpei Tang:** Project administration, Validation. **Feitai Chen:** Project administration, Validation. **Haiyan Zhang:** Experimental, Conceptualization, Methodology. **Zi Zhu:** Experimental, Conceptualization, Methodology.

Declaration of Competing Interest

The authors declare that they have no known competing financial interests or personal relationships that could have appeared to influence the work reported in this paper.

Acknowledgements

We thank the National Natural Science Foundation of China (21763010, 52072146, 22005117), Project Fund of Jishou University (Jdy21082), Key Laboratory of Mineral Cleaner Production, and Exploit of Green Functional Materials in Hunan Province for providing funding. We thank Simon Partridge, PhD, from Liwen Bianji, Edanz Editing China (<http://www.liwenbianji.cn/>), for editing the English text of a draft of this manuscript.

Appendix A. Supporting information

Supplementary data associated with this article can be found in the online version at [doi:10.1016/j.apcatb.2022.121065](https://doi.org/10.1016/j.apcatb.2022.121065).

References

- [1] S. Chu, A. Majumdar, Opportunities and challenges for a sustainable energy future, *Nature* 488 (2012) 294–303.
- [2] Q. Guo, L. Fu, T. Yan, W. Tian, D. Ma, J. Li, Y. Jiang, X. Wang, Improved photocatalytic activity of porous ZnO nanosheets by thermal deposition graphene-like g-C₃N₄ for CO₂ reduction with H₂O vapor, *Appl. Surf. Sci.* 509 (2020), 144773.
- [3] D.U. Nielsen, X.-M. Hu, K. Daasbjerg, T. Skrydstrup, Chemically and electrochemically catalysed conversion of CO₂ to CO with follow-up utilization to value-added chemicals, *Nat. Catal.* 1 (2018) 244–254.
- [4] D.O. Adekoya, M. Tahir, N.A.S. Amin, g-C₃N₄/(Cu/TiO₂) nanocomposite for enhanced photoreduction of CO₂ to CH₃OH and HCOOH under UV/visible light, *J. CO₂ Util.* 18 (2017) 261–274.
- [5] E.V. Kondratenko, G. Mul, J. Baltrusaitis, G.O. Larrazábal, J. Pérez-Ramírez, Status and perspectives of CO₂ conversion into fuels and chemicals by catalytic, photocatalytic and electrocatalytic processes, *Energy Environ. Sci.* 6 (2013) 3112–3135.
- [6] T. Inoue, A. Fujishima, S. Konishi, K.J.N. Honda, Photoelectrocatalytic reduction of carbon dioxide in aqueous suspensions of semiconductor powders, *Nature* 277 (1979) 637–638.
- [7] X. Chang, T. Wang, J. Gong, CO₂ photo-reduction: insights into CO₂ activation and reaction on surfaces of photocatalysts, *Energy Environ. Sci.* 9 (2016) 2177–2196.
- [8] Y. Wang, Z. Zhang, L. Zhang, Z. Luo, J. Shen, H. Lin, J. Long, J.C.S. Wu, X. Fu, X. Wang, C. Li, Visible-light driven overall conversion of CO₂ and H₂O to CH₄ and O₂ on 3D-SiC@2D-MoS₂ heterostructure, *J. Am. Chem. Soc.* 140 (2018) 14595–14598.
- [9] L. Liu, H. Zhao, J.M. Andino, Y. Li, Photocatalytic CO₂ reduction with H₂O on TiO₂ nanocrystals: comparison of anatase, rutile, and brookite polymorphs and exploration of surface chemistry, *ACS Catal.* 2 (2012) 1817–1828.
- [10] Y. Jo, C. Kim, G.-H. Moon, J. Lee, T. An, W. Choi, Activation of peroxymonosulfate on visible light irradiated TiO₂ via a charge transfer complex path, *Chem. Eng. J.* 346 (2018) 249–257.
- [11] C. Wang, R.L. Thompson, P. Ohodnicki, J. Baltrus, C. Matranga, Size-dependent photocatalytic reduction of CO₂ with PbS quantum dot sensitized TiO₂ heterostructured photocatalysts, *J. Mater. Chem.* 21 (2011) 13452–13457.
- [12] G. Zeng, J. Qiu, Z. Li, P. Pavaskar, S.B. Cronin, CO₂ reduction to methanol on TiO₂-passivated GaP photocatalysts, *ACS Catal.* 4 (2014) 3512–3516.
- [13] L. Huang, B. Li, B. Su, Z. Xiong, C. Zhang, Y. Hou, Z. Ding, S. Wang, Fabrication of hierarchical Co₃O₄@CdIn₂S₄ p–n heterojunction photocatalysts for improved CO₂ reduction with visible light, *J. Mater. Chem. A* 8 (2020) 7177–7183.
- [14] Q. Gao, J. Xu, Z. Wang, Y. Zhu, Enhanced visible photocatalytic oxidation activity of perylene diimide/g-C₃N₄ n–n heterojunction via π - π interaction and interfacial charge separation, *Appl. Catal. B-Environ.* 271 (2020), 118933.
- [15] J.C. Wang, H.C. Yao, Z.Y. Fan, L. Zhang, J.S. Wang, S.Q. Zang, Z.J. Li, Indirect Z-scheme BiOI/g-C₃N₄ photocatalysts with enhanced photoreduction CO₂ activity under visible light irradiation, *ACS Appl. Mater. Inter.* 8 (2016) 3765–3775.
- [16] J. Yu, K. Wang, W. Xiao, B. Cheng, Photocatalytic reduction of CO₂ into hydrocarbon solar fuels over g-C₃N₄-Pt nanocomposite photocatalysts, *PCPP* 16 (2014) 11492–11501.
- [17] M. Zhou, S. Wang, P. Yang, Z. Luo, R. Yuan, A.M. Asiri, M. Wakeel, X. Wang, Layered heterostructures of ultrathin polymeric carbon nitride and ZnIn₂S₄ nanosheets for photocatalytic CO₂ reduction, *Chem. Eur. J.* 24 (2018) 18529–18534.
- [18] L. Mohapatra, K. Parida, A review on the recent progress, challenges and perspective of layered double hydroxides as promising photocatalysts, *J. Mater. Chem. A* 4 (2016) 10744–10766.
- [19] P.J. Sideris, U.G. Nielsen, Z. Gan, C.P. Grey, Mg/Al ordering in layered double hydroxides revealed by multinuclear NMR spectroscopy, *Science* 321 (2008) 113–117.
- [20] N. Ahmed, Y. Shibata, T. Taniguchi, Y. Izumi, Photocatalytic conversion of carbon dioxide into methanol using zinc–copper–M(III) (M=aluminum, gallium) layered double hydroxides, *J. Catal.* 279 (2011) 123–135.
- [21] Z. Gu, J.J. Atherton, Z.P. Xu, Hierarchical layered double hydroxide nanocomposites: structure, synthesis and applications, *Chem. Commun.* 51 (2015) 3024–3036.
- [22] Y. Zhao, X. Jia, G.I.N. Waterhouse, L.-Z. Wu, C.-H. Tung, D. O'Hare, T. Zhang, Layered double hydroxide nanostructured photocatalysts for renewable energy production, *Adv. Energy Mater.* 6 (2016), 1501974.
- [23] T. Ye, W. Huang, L. Zeng, M. Li, J. Shi, CeO₂-x platelet from monometallic cerium layered double hydroxides and its photocatalytic reduction of CO₂, *Appl. Catal. B-Environ.* 210 (2017) 141–148.
- [24] M. Moradi, F. Hasanvandian, A.A. Isari, F. Hayati, B. Kakavandi, S.R. Setayesh, CuO and ZnO co-anchored on g-C₃N₄ nanosheets as an affordable double Z-scheme nanocomposite for photocatalytic decontamination of amoxicillin, *Appl. Catal. B Environ.* 285 (2021), 119838.
- [25] J. Xu, Z. Wang, Y. Zhu, Highly efficient visible photocatalytic disinfection and degradation performances of microtubular nanoporous g-C₃N₄ via hierarchical construction and defects engineering, *J. Mater. Sci. Technol.* 49 (2020) 133–143.
- [26] K. Wang, Q. Li, B. Liu, B. Cheng, W. Ho, J. Yu, Sulfur-doped g-C₃N₄ with enhanced photocatalytic CO₂-reduction performance, *Appl. Catal. B-Environ.* 176–177 (2015) 44–52.
- [27] P. Huang, J. Huang, S.A. Pantovich, A.D. Carl, T.G. Fenton, C.A. Caputo, R. L. Grimm, A.I. Frenkel, G. Li, Selective CO₂ reduction catalyzed by single cobalt sites on carbon nitride under visible-light irradiation, *J. Am. Chem. Soc.* 140 (2018) 16042–16047.
- [28] Q. Xiang, J. Yu, M. Jaroniec, Preparation and enhanced visible-light photocatalytic H₂-production activity of graphene/C₃N₄ composites, *J. Phys. Chem. C* 115 (2011) 7355–7363.
- [29] S. Tonda, S. Kumar, M. Bhardwaj, P. Yadav, S. Ogale, g-C₃N₄/NiAl-LDH 2D/2D hybrid heterojunction for high-performance photocatalytic reduction of CO₂ into renewable fuels, *ACS Appl. Mater. Inter.* 10 (2018) 2667–2678.
- [30] L. Zhang, M. Ou, H. Yao, Z. Li, D. Qu, F. Liu, J. Wang, Z. Li, Enhanced supercapacitive performance of graphite-like C₃N₄ assembled with NiAl-layered double hydroxide, *Electrochim. Acta* 186 (2015) 292–301.
- [31] S. Nayak, L. Mohapatra, K. Parida, Visible light-driven novel g-C₃N₄/NiFe-LDH composite photocatalyst with enhanced photocatalytic activity towards water oxidation and reduction reaction, *J. Mater. Chem. A* 3 (2015) 18622–18635.
- [32] X. Zhao, X. Zhao, I. Ullah, L. Gao, J. Zhang, J. Lu, The In-situ growth NiFe-layered double hydroxides/g-C₃N₄ nanocomposite 2D/2D heterojunction for enhanced photocatalytic CO₂ reduction performance, *Catal. Lett.* 151 (2020) 1683–1692.
- [33] W. Wan, S. Yu, F. Dong, Q. Zhang, Y. Zhou, Efficient C₃N₄/graphene oxide macroscopic aerogel visible-light photocatalyst, *J. Mater. Chem. A* 4 (2016) 7823–7829.
- [34] Y. Yang, J. Wu, T. Xiao, Z. Tang, J. Shen, H. Li, Y. Zhou, Z. Zou, Urchin-like hierarchical CoZnAl-LDH/RGO/g-C₃N₄ hybrid as a Z-scheme photocatalyst for efficient and selective CO₂ reduction, *Appl. Catal. B-Environ.* 255 (2019), 117771.
- [35] C. Li, Y. Dou, J. Liu, Y. Chen, S. He, M. Wei, D.G. Evans, X. Duan, Synthesis of supported Ni@Rh(Ni-alloy) nanocomposites as an efficient catalyst towards hydrogen generation from N₂H₄BH₃, *Chem. Commun.* 49 (2013) 9992–9994.
- [36] Y.Y. Du, Q. Jin, J.T. Feng, N. Zhang, Y.F. He, D.Q. Li, Flower-like Au/Ni-Al hydrotalcite with hierarchical pore structure as a multifunctional catalyst for catalytic oxidation of alcohol, *Catal. Sci. Technol.* 5 (2015) 3216–3225.
- [37] S. Tonda, S. Kumar, Y. Gawli, M. Bhardwaj, S. Ogale, g-C₃N₄ (2D)/CdS (1D)/RGO (2D) dual-interface nano-composite for excellent and stable visible light photocatalytic hydrogen generation, *Int. J. Hydrog. Energy* 42 (2017) 5971–5984.

- [38] Y. Sheng, W. Li, Y. Zhu, L. Zhang, Ultrathin perylene imide nanosheet with fast charge transfer enhances photocatalytic performance, *Appl. Catal. B Environ.* 298 (2021), 120585.
- [39] L. Mohapatra, D. Patra, K. Parida, S.J. Zaidi, Enhanced photocatalytic activity of a molybdate-intercalated iron-based layered double hydroxide, *Eur. J. Inorg. Chem.* 3 (2017) 723–733.
- [40] K.S. Sing, Reporting physisorption data for gas/solid systems with special reference to the determination of surface area and porosity (recommendations 1984), *Pure Appl. Chem.* 57 (1985) 603–619.
- [41] S. Tonda, S. Kumar, S. Kandula, V. Shanker, Fe-doped and -mediated graphitic carbon nitride nanosheets for enhanced photocatalytic performance under natural sunlight, *J. Mater. Chem. A* 2 (2014) 6772–6780.
- [42] F. Fina, S.K. Callear, G.M. Carins, J.T.S. Irvine, Structural investigation of graphitic carbon nitride via XRD and neutron diffraction, *Chem. Mater.* 27 (2015) 2612–2618.
- [43] G. Salehi, R. Abazari, A.R. Mahjoub, Visible-light-induced graphitic-C₃N₄@Nickel-Aluminum layered double hydroxide nanocomposites with enhanced photocatalytic activity for removal of dyes in water, *Inorg. Chem.* 57 (2018) 8681–8691.
- [44] M.Y. Miao, J.T. Feng, Q. Jin, Y.F. He, Y.N. Liu, Y.Y. Du, N. Zhang, D.Q. Li, Hybrid Ni–Al layered double hydroxide/graphene composite supported gold nanoparticles for aerobic selective oxidation of benzyl alcohol, *RSC Adv.* 5 (2015) 36066–36074.
- [45] S. Kumar, M.A. Isaacs, R. Trofimovaite, L. Durnell, C.M.A. Parlett, R. E. Douthwaite, B. Coulson, M.C.R. Cockett, K. Wilson, A.F. Lee, P25@CoAl layered double hydroxide heterojunction nanocomposites for CO₂ photocatalytic reduction, *Appl. Catal. B-Environ.* 209 (2017) 394–404.
- [46] J. Chen, B. Yao, C. Li, G. Shi, An improved Hummers method for eco-friendly synthesis of graphene oxide, *Carbon* 64 (2013) 225–229.
- [47] J.I. Paredes, S. Villar-Rodil, P. Solis-Fernandez, A. Martinez-Alonso, J.M. Tascon, Atomic force and scanning tunneling microscopy imaging of graphene nanosheets derived from graphite oxide, *Langmuir* 25 (2009) 5957–5968.
- [48] J. Fu, B. Zhu, C. Jiang, B. Cheng, W. You, J. Yu, Hierarchical porous O-doped g-C₃N₄ with enhanced photocatalytic CO₂ reduction activity, *Small* 13 (2017), 1603938.
- [49] F. Zhang, Y. Song, S. Song, R. Zhang, W. Hou, Synthesis of magnetite-graphene oxide-layered double hydroxide composites and applications for the removal of Pb (II) and 2,4-dichlorophenoxyacetic acid from aqueous solutions, *ACS Appl. Mater. Inter.* 7 (2015) 7251–7263.
- [50] Y. Wang, X. Bai, H. Qin, F. Wang, Y. Li, X. Li, S. Kang, Y. Zuo, L. Cui, Facile one-step synthesis of hybrid graphitic carbon nitride and carbon composites as high-performance catalysts for CO₂ photocatalytic conversion, *ACS Appl. Mater. Inter.* 8 (2016) 17212–17219.
- [51] M. Zhang, X. Wang, Two dimensional conjugated polymers with enhanced optical absorption and charge separation for photocatalytic hydrogen evolution, *Energy Environ. Sci.* 7 (2014) 1902–1906.
- [52] W.K. Jo, Y.G. Kim, S. Tonda, Hierarchical flower-like NiAl-layered double hydroxide microspheres encapsulated with black Cu-doped TiO₂ nanoparticles: Highly efficient visible-light-driven composite photocatalysts for environmental remediation, *J. Hazard. Mater.* 357 (2018) 19–29.
- [53] X. Lu, J. Ma, H. Jiang, C. Liu, K.M. Lau, Low trap states in in situ SiNx/AlN/GaN metal-insulator-semiconductor structures grown by metal-organic chemical vapor deposition, *Appl. Phys. Lett.* 105 (2014), 102911.
- [54] W.-K. Jo, S. Moru, S. Tonda, A green approach to the fabrication of a TiO₂/NiAl-LDH core-shell hybrid photocatalyst for efficient and selective solar-powered reduction of CO₂ into value-added fuels, *J. Mater. Chem. A* 8 (2020) 8020–8032.
- [55] C. Rudolf, B. Dragoi, A. Ungureanu, A. Chiriac, S. Royer, A. Nastro, E. Dumitriu, NiAl and CoAl materials derived from takovite-like LDHs and related structures as efficient chemoselective hydrogenation catalysts, *Catal. Sci. Technol.* 4 (2014) 179–189.
- [56] J. Klopogge, R.J.R. Frost, V. (Eds.), *Layered Double Hydroxides: Present and Future*, Nova Publishers, 2001, pp. 153–215.
- [57] W.-K. Jo, S. Kumar, S. Tonda, N-doped C dot/CoAl-layered double hydroxide/g-C₃N₄ hybrid composites for efficient and selective solar-driven conversion of CO₂ into CH₄, *Compos. Part B-Eng.* 176 (2019), 107212.
- [58] J. Ni, J. Xue, L. Xie, J. Shen, G. He, H. Chen, Construction of magnetically separable NiAl LDH/Fe₃O₄-RGO nanocomposites with enhanced photocatalytic performance under visible light, *PCCP* 20 (2017) 414–421.
- [59] J. Liqiang, Q. Yichun, W. Baiqi, L. Shudan, J. Baojiang, Y. Libin, F. Wei, F. Honggang, S. Jiazhong, Review of photoluminescence performance of nano-sized semiconductor materials and its relationships with photocatalytic activity, *Sol. Energy Mater. Sol. Cells* 90 (2006) 1773–1787.
- [60] B. Li, W. Peng, J. Zhang, J.C. Lian, T. Huang, N. Cheng, Z. Luo, W.Q. Huang, W. Hu, A. Pan, L. Jiang, G.F. Huang, High-throughput one-photon excitation pathway in 0D/3D heterojunctions for visible-light driven hydrogen evolution, *Adv. Funct. Mater.* 31 (2021), 2100816.
- [61] F. Xu, K. Meng, B. Cheng, S. Wang, J. Xu, J. Yu, Unique S-scheme heterojunctions in self-assembled TiO₂/CsPbBr₃ hybrids for CO₂ photoreduction, *Nat. Commun.* 11 (2020) 1–9.
- [62] J. Bian, Q. Li, C. Huang, J. Li, Y. Guo, M. Zaw, R.-Q. Zhang, Thermal vapor condensation of uniform graphitic carbon nitride films with remarkable photocurrent density for photoelectrochemical applications, *Nano Energy* 15 (2015) 353–361.
- [63] M. Yang, P. Wang, S. Tang, F. Chen, Y. Li, Preparation of cellular C₃N₄/CoSe₂/GA composite photocatalyst and its CO₂ reduction activity, *Chem. J. Chin. U* 42 (2021) 1924–1932 (in Chinese).
- [64] X. Xiong, Y. Zhao, R. Shi, W. Yin, Y. Zhao, G.I.N. Waterhouse, T. Zhang, Selective photocatalytic CO₂ reduction over Zn-based layered double hydroxides containing tri or tetravalent metals, *Sci. Bull.* 65 (2020) 987–994.
- [65] C. Sun, Y. Liu, Z. Wang, P. Wang, Z. Zheng, H. Cheng, X. Qin, X. Zhang, Y. Dai, B. Huang, Self-assembled g-C₃N₄ nanotubes/graphdiyne composite with enhanced photocatalytic CO₂ reduction, *J. Alloy. Compd.* 868 (2021), 159045.
- [66] Y. Zhao, G. Chen, T. Bian, C. Zhou, G.I. Waterhouse, L.Z. Wu, C.H. Tung, L.J. Smith, D. O'Hare, T. Zhang, Defect-rich ultrathin ZnAl-layered double hydroxide nanosheets for efficient photoreduction of CO₂ to CO with water, *Adv. Mater.* 27 (2015) 7824–7831.
- [67] Y.Y. Li, Z.H. Wei, J.B. Fan, Z.J. Li, H.C. Yao, Photocatalytic CO₂ reduction activity of Z-scheme CdS/CdWO₄ catalysts constructed by surface charge directed selective deposition of CdS, *Appl. Surf. Sci.* 483 (2019) 442–452.
- [68] M. Xu, C. Sun, X. Zhao, H. Jiang, H. Wang, P. Huo, Fabricated hierarchical CdS/Ni-MOF heterostructure for promoting photocatalytic reduction of CO₂, *Appl. Surf. Sci.* 576 (2022), 151792.
- [69] X. Jiao, X. Li, X. Jin, Y. Sun, J. Xu, L. Liang, Y. Xie, Partially oxidized SnS₂ atomic layers achieving efficient visible-light-driven CO₂ reduction, *J. Am. Chem. Soc.* 139 (2017) 18044–18051.
- [70] L. Li, C. Guo, J. Ning, Y. Zhong, D. Chen, Y. Hu, Oxygen-vacancy-assisted construction of FeOOH/CdS heterostructure as an efficient bifunctional photocatalyst for CO₂ conversion and water oxidation, *Appl. Catal. B Environ.* 293 (2021), 120203.
- [71] J. Wang, Y. Wang, M. Yu, G. Li, S. Zhang, Q. Zhong, Formation of flaky carbon nitride and beta-Indium sulfide heterojunction with efficient separation of charge carriers for enhanced photocatalytic carbon dioxide reduction, *J. Colloid Interface Sci.* 21 (2021) 02217–02217.
- [72] X. Chen, J. Wang, Y. Chai, Z. Zhang, Y. Zhu, Efficient photocatalytic overall water splitting induced by a giant internal electric field of g-C₃N₄/rGO/PDIP Z-scheme heterojunction, *Adv. Mater.* 33 (2021), 2007479.
- [73] M. Humayun, H. Ullah, J. Cao, W. Pi, Y. Yuan, S. Ali, Experimental and DFT studies of Au deposition over WO₃/g-C₃N₄ Z-scheme heterojunction, *Nano Micro Lett.* 12 (2020) 1–18.
- [74] F. Guo, W. Shi, H. Wang, M. Han, H. Li, H. Huang, Z. Kang, Facile fabrication of a CoO/g-C₃N₄ p–n heterojunction with enhanced photocatalytic activity and stability for tetracycline degradation under visible light, *Catal. Sci. Technol.* 15 (2017) 3325–3331.
- [75] Z. Jiang, W. Wan, H. Li, S. Yuan, H. Zhao, P.K. Wong, A hierarchical Z-scheme alpha-Fe₂O₃/g-C₃N₄ hybrid for enhanced photocatalytic CO₂ reduction, *Adv. Mater.* 30 (2018), 1706108.
- [76] J. Sheng, Y. He, J. Li, C. Yuan, H. Huang, S. Wang, Y. Sun, Z. Wang, F. Dong, Identification of halogen-associated active sites on bismuth-based perovskite quantum dots for efficient and selective CO₂-to-CO photoreduction, *ACS Nano* 14 (2020) 13103–13114.
- [77] X. Li, Y. Sun, J. Xu, Y. Shao, J. Wu, X. Xu, Y. Pan, H. Ju, J. Zhu, Y. Xie, Selective visible-light-driven photocatalytic CO₂ reduction to CH₄ mediated by atomically thin CuIn₂S₃ layers, *Nat. Energy* 4 (2019) 690–699.
- [78] Y. Li, B. Li, D. Zhang, L. Cheng, Q. Xiang, Crystalline carbon nitride supported copper single atoms for photocatalytic CO₂ reduction with nearly 100% CO selectivity, *ACS Nano* 14 (2020) 10552–10561.
- [79] T. Wang, X. Meng, P. Li, S. Ouyang, K. Chang, G. Liu, Z. Mei, J. Ye, Photoreduction of CO₂ over the well-crystallized ordered mesoporous TiO₂ with the confined space effect, *Nano. Energy* 9 (2014) 50–60.
- [80] J.-y Tang, R.-t Guo, W.-g Zhou, C.-y Huang, W.-g Pan, Ball-flower like NiO/g-C₃N₄ heterojunction for efficient visible light photocatalytic CO₂ reduction, *Appl. Catal. B Environ.* 237 (2018) 802–810.